Sedimentation dynamics of triply twisted Möbius bands: Geometry versus topology

Nicolás Moreno [*]
CFD-MS, Basque Center for Applied Mathematics, Alameda de Mazarredo 14, Bilbao 48009, Bizkaia, Spain

David Vázquez-Cortés and Eliot Fried [†]
Materials and Mechanics Unit, Okinawa Institute of Science and Technology, 1919-1 Tancha, Onna-son 904-0495, Okinawa, Japan

(Received 18 March 2024; accepted 22 July 2024; published 6 August 2024)

We explore the sedimentation dynamics of triply twisted Möbius bands, each characterized by threefold rotational symmetry but distinguished by its construction and intrinsic geometrical properties. Three types of bands are considered: one with vanishing Gaussian curvature, constructed by isometrically deforming flat rectangular strips through bending without stretching; and two with negative Gaussian curvature, one being constructed by isometrically deforming helicoids. Experiment on these three types of bands, with a focus on varying aspect ratios, reveals a singular phenomenon: while the spin directions of bands not derived from helicoids spin in directions consistent with their inherent chirality, bands derived from helicoids exhibit an aspect-ratio-dependent spin, pointing to the existence of a critical aspect ratio at which geometric factors dominate over chiral influences. Supported by numerical simulations and a detailed analysis of the resistance tensors, we propose the unique response of bands derived from helicoids originates from a complex interaction among geometry, topology, and hydrodynamics. Two explanations are offered for the chiral transition observed in bands derived from helicoid. First, this transition may parallel the dynamics of superhelices, for which competing chiralities influence rotational behavior. Second, the unique geometrical properties of bands derived from helicoids, coupled with deviations between the rotation axis and the local symmetry axis, may underlie the observed aspect-ratio-dependent chiral transition. Our study underscores the significant role of geometrical and topological nuances in determining the behavior of chiral objects suspended in fluids. In addition to offering transformative potential across diverse fields, it promises advancements in mixing, separation processes, and innovative passive swimmers.

DOI: 10.1103/PhysRevResearch.6.033141

I. INTRODUCTION

The hydrodynamics of falling objects has long intrigued researchers in the field of fluid mechanics, as understanding the intricate interactions between a body and the fluid through which it moves is fundamental to various natural and engineered systems. Factors such as body shape, periodic and oscillatory motions, and complex fluid-structure interactions play critical roles in this phenomenon [1]. These factors are particularly important for understanding various phenomena, including the flight of insects [2], the dispersal mechanisms of tree seeds [3], meteorological patterns [4], and sediment transport in aquatic environments [5]. Investigating the interactions between these effects provides insights into the fundamental principles of fluid dynamics and their practical applications to natural processes and the improvement of technological designs. In the last decade, researchers have successfully manufactured novel materials with tailored chirality [6–9] as evidenced by their diverse applications in chiral sensing [10], separation [11], catalysis [12], and flow-driven rotatory motors [8,13]. From a theoretical standpoint, understanding how chiral objects respond to different external physical stimuli poses significant challenges. As a result, there has been considerable interest in studying the hydrodynamic behavior of chiral objects in fluids. A notable finding from these studies is the tendency of chiral objects with different handedness to rotate in opposite directions during sedimentation. This phenomenon has been applied in enantiomer classification and separation [14–16]. However, the experimental and simulation evidence we present challenges the notion that this behavior universally applies to all chiral objects.

In a low Reynolds number regime, a rigid body moving in an incompressible, viscous liquid experiences hydrodynamic forces and torques, leading to translation and rotation. The coupling of these motions depends on the geometry and topology of the body. For instance, a screwlike rigid body rotating in a quiescent fluid imparts linear motion relative to the fluid, generating a force, and simultaneously induces torque, leading to vortical motion in the liquid [17–23]. Similar phenomena are observed in biological structures, where chirality is linked to form [24]. As the Reynolds number

[*]Contact author: nmoreno@bcamath.org
[†]Contact author: eliot.fried@oist.jp

increases within the laminar range (say from 10^2 to 4×10^2), wake formation and other hydrodynamic effects can give rise to intricate oscillatory trajectories of the body [1,19]. In shear flows, helical particles can display a passive drifting motion. This behavior occurs alongside the well-documented Jeffery orbits, which are characteristic of elongated particles. The drifting of helical particles is attributed to effects induced by their chiral nature [25]. The stability of these trajectories is intricately linked to the specific geometrical and topological attributes of the considered body.

Happel and Brenner provided a concise framework for characterizing the dynamics of an arbitrarily shaped rigid body moving in a viscous incompressible liquid [26] at low Reynolds numbers. Given a point o affixed to the body, let $\boldsymbol{v}_o$ be the instantaneous velocity of that point, and let $\boldsymbol{\omega}$ be the instantaneous angular velocity of the body about that point. The net force $\boldsymbol{f}$ and net hydrodynamic torque $\boldsymbol{\tau}_o$ exerted by the liquid on the body are then given by

$$\begin{bmatrix} \boldsymbol{f} \\ \boldsymbol{\tau}_o \end{bmatrix} = -\mu \mathbb{R} \begin{bmatrix} \boldsymbol{v}_o \\ \boldsymbol{\omega} \end{bmatrix}, \quad \mathbb{R} = \begin{bmatrix} \mathbf{K} & \mathbf{C}_o^\top \\ \mathbf{C}_o & \boldsymbol{\Omega}_o \end{bmatrix}, \tag{1}$$

where μ is the viscosity of the liquid and $\mathbf{K}$, $\boldsymbol{\Omega}_o$, and $\mathbf{C}_o$ are the translation, rotation, and the coupling dyads. While $\mathbf{K}$ is an intrinsic property determined entirely by the geometry and topology of the body, $\boldsymbol{\Omega}_o$ and $\mathbf{C}_o$ depend also on the choice of the origin o. The dyads $\mathbf{K}$ and $\boldsymbol{\Omega}_o$ are necessarily symmetric and positive definite. Although $\mathbf{C}_o$ is generally asymmetric, the resistance tensor $\mathbb{R}$ is consequently symmetric and positive definite. For a chiral body $\mathbb{R}$ encodes its preferred spinning direction [17,27,28].

Chiral bodies generally exhibit more complex behaviors than their achiral counterparts, owing to induced hydrodynamic interactions that arise from their handedness. The impact of these chiral characteristics has been explored through various theoretical and experimental studies [29]. As the Reynolds number increases, additional inertial effects can lead to more complex dynamics due to wake formation rendering the behavior of chiral objects even more intricate [1].

II. MATERIALS AND METHODS

A. Construction of triply twisted Möbius bands

A Möbius band is an emblematic chiral structure that can be made by connecting the ends of a strip after applying an odd number of twists. Here, we examine three distinct families of triply twisted, threefold symmetric Möbius bands, investigating the variability of their intrinsic chiral response within each family based on two dimensionless parameters: a notion of aspect ratio that we define subsequently and the Archimedes number Ar (the ratio of gravitational forces to viscous forces). Möbius bands can be constructed in various ways. One approach includes bending a rectangular strip of length L and width w into a sequence of three helical sections linked by planar segments [30], as illustrated in Fig. 1. Any such band is developable, meaning that it can be isometrically flattened without stretching, contraction, folding, or tearing. We use D to denote the family of ruled triply twisted Möbius bands constructed in this way. We also consider rotoidal bands, constructed by uniformly translating a line segment of length w along a circle with a radius of $L/2\pi$, while simultaneously rotating it at a twist rate of $\omega_{\text{twist}} = \pm 3\pi/L$ [31], as illustrated in Fig. 1. To ensure the resulting surface remains free from self-intersections, we require that $w < L/\pi$. These bands belong to the family denoted as R as illustrated in Fig. 1. We also consider a class of ruled, triply twisted, threefold symmetric Möbius bands which arise as the limiting surfaces of closed kinematic chains known as Möbius kaleidocycles, similar to the binormal-scroll (B) bands [32]. These Möbius bands are isometric deformations of helicoids [33], exclusively attainable through bending and twisting, without involving any stretching or contraction. While each Möbius band considered has the same topology and has threefold rotational symmetry, each family of Möbius bands has distinct features, which we describe in the next two paragraphs.

The dynamics of a rigid body sedimenting in a liquid are significantly influenced by the angles at which the liquid strikes the body. It is therefore important to consider the projected area in the direction of the motion and curvature of the sedimenting body as pivotal factors. While maintaining a fixed aspect ratio, the projected area can differ across the three families of bands considered. To enable a meaningful comparison, we introduce the projected radius R, which corresponds to the radius of the circle inscribing the projected midline of a band as observed in Fig. 1 [see also Supplemental Material (SM) [34], Fig. 2]. The projected midline takes the form of a triangular loop for bands of type D, a circle for bands of type R, and what resembles a Reuleaux for bands of type B, as illustrated in Fig. 1 and SM [34], Fig. 3. We consider it noteworthy that for a constant R, bands of type D are more compact than bands of type B with the same aspect ratio, whereas bands of type B are notably more compact than R counterparts with the same aspect ratio. In a broader sense, bands of type R can achieve higher aspect ratios because their circular midlines provide more internal space within the loop. Conversely, bands of type D and B are expected to have smaller aspect ratios owing to their relatively confined inner available space. Considering the curvature characteristics of the bands, bands of type B and D differ due to disparities in the rates at which their rulings rotate around their midlines. Specifically, bands of type D exhibit zero Gaussian curvature ($K = 0$) and comprise three straight segments where rotation rates are null. In contrast, bands of type B and R share negative Gaussian curvature ($K < 0$) attributed to the constant twist of the generatrix, which we denote by ω_{twist} ($8.0941/L$ [32] and $3\pi/(L)$ for bands of type B and R, respectively). We speculate that bands of type B amalgamate select geometrical properties from bands of type D and R in novel ways, underpinning their behavior during sedimentation. Moreover, these distinctions influence the resistance tensor of bands of type B, leading to intricate chiral transitions in their hydrodynamic response.

B. Sedimentation studies

We conducted comprehensive sedimentation studies, encompassing both experimental and numerical investigations, focusing on triply twisted bands. These threefold symmetric bands are characterized by their projected radius R, width w, and mass density ρ_s. Sedimentation occurred in an

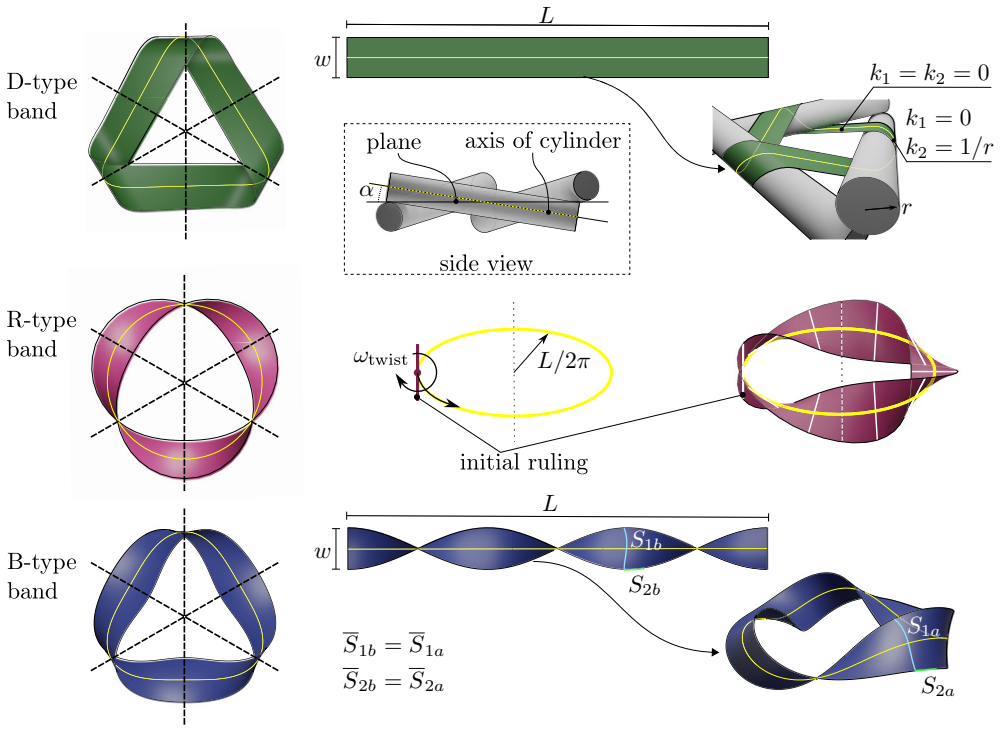

FIG. 1. Triply twisted, threefold symmetric Möbius bands and their construction. Bands of type D (developable) are constructed by bending a rectangular strip of length L and width w around three cylinders of radius r, and angle α between them. The principal curvatures k_1 and k_2 are also shown for the different sections of the band. Bands of type rotoidal R (rotoidal) are constructed by moving a line segment, from its middle point, around a circle of radius $L/2\pi$ while turning it perpendicular to the movement at a rate twist of $\omega_{\text{twist}} = 3\pi/L$. Construction of bands of type B (binormal scroll) are created by isometrically bending a helicoid, as explained in Ref. [33]. Consequently, the length of curves S_{1b} and S_{2b} on the helicoid remains unchanged after forming the triply twisted Möbius band. The midline of each type of bands is presented in yellow.

incompressible, viscous liquid with mass density ρ and shear viscosity μ. The width w of the bands varied among different cases to explore the effects of aspect ratio. In Fig. 2, we provide an illustration of the sedimentation setup and the various motions experienced by the bands during the experiments. Our experimental studies used three-dimensional (3D)-printed polystyrene bands, each with $R = 1$ cm, sedimenting in water. See Supplemental Material [34] for samples of stl files used to print the bands. Further details on the experimental setup can be found in the Appendix A. In this context, the forces influencing the bands include the force due to gravity, the buoyancy force, and the drag force. As each band descends, it eventually reaches a terminal velocity v_z, measured with respect to a reference frame located at the top of the container. Additionally, they exhibit an angular velocity, ω_{cm}, relative to a moving frame fixed on the center of mass of each band and aligned with a suitably chosen frame of reference determined by the container. The instantaneous orientation of a band can be described by an orthonormal vector triad, with each vector originating from the center of mass of the band. Assuming that the vector connecting a marker F to the center of mass is aligned with one of the vectors in the triad lying on the x-y plane as shown in Fig. 2, the angles ϕ and Ψ can be used to determine the angular velocity $\omega_{\text{cm}} = \dot{\phi}$ and the tumbling angle Ψ. The existence of tumbling can induce differences with the actual value of ϕ. However, since the variations observed in Ψ are consistently small it provides a good approximation to the rotational velocity. The sign for spinning direction or chiral response is designated as positive $(+)$ when the band rotates counterclockwise, as observed from a top-down perspective. We define the term chiral transition as a change in spinning direction for bands in the same family when the aspect ratio of the bands change. We also define the geometric or intrinsic chirality of the bands based on the direction of twist (w_{twist}). For further clarification, please refer to SM [34], Fig. 1, which includes an illustrative example contrasting two different enantiomers derived from the same midline.

To facilitate a comparative study of the influence of aspect ratio w/R across the three types of Möbius bands, we introduce the parameter $\chi = w/w_{\text{max}}$, with w_{max} representing the width (w) when the edges touch at the center (details provided in SM [34], Fig. 2). Bands of type R, characterized by higher attainable aspect ratios w/R, exhibit the maximum surface area among the bands investigated. For bands of type B and R, χ varies within the range $0.1 \leqslant \chi \leqslant 1$. In comparison, the construction of bands of type D involves two additional parameters: the radius r of the three cylinders about which the curved sections of the band are wrapped, and the angle α between these cylinders [30], as illustrated in Fig. 1. To streamline our investigation, we set $\chi = 0.6$ and $\chi = 0.8$ for bands of type D while allowing for variations of the cylinders angle.

A rigid object sedimenting in a fluid can be characterized in terms of three parameters [1], (i) the density ratio $(\rho - \rho_s)/\rho$

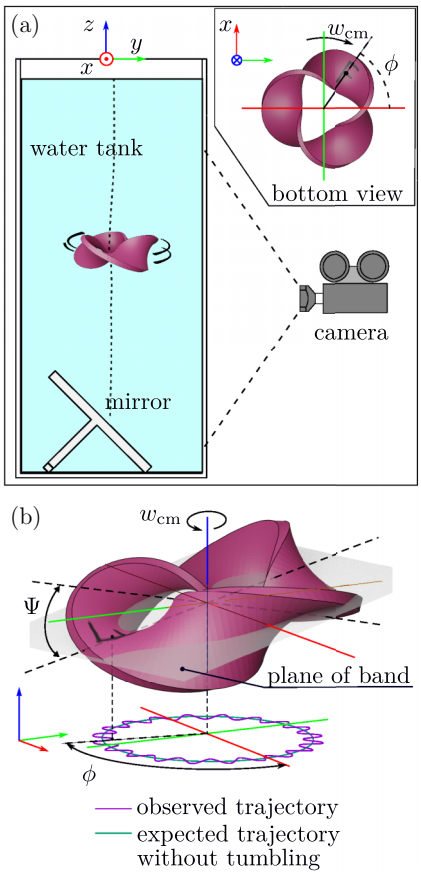

FIG. 2. Schematic of experimental setup to study the sedimentation of triply twisted Möbius bands. (a) In the base of a water tank with a square cross-sectional area, a mirror is positioned. The camera in front of the water tank allows us to directly observe the movement of Möbius bands in the (x, z) plane during sedimentation. The mirror at the bottom of the tank allows us to observe the movements of the bands in the (x, y) plane as sketched in the bottom-view inset. (b) The Möbius band rotates at angular velocity $\omega_{cm} = \dot{\phi}$ and tumble at angle Ψ. ϕ is the angle formed by the red axis and the projection in the (x, y) plane of the line segment connecting the center of gravity of the band and the position of the marker "F". The red, green, and blue axis are parallel to the x, y, and z axis, respectively, and pass through the center of mass of the band.

between the object and the fluid; (ii) a set of geometrical parameters that defines the anisotropy of the body; and (iii) the Archimedes number $\mathrm{Ar} = \rho(\rho - \rho_s)gR^3/\mu^2$. In our study, the density ratio is fixed by the material of the bands and the fluid, and the aspect ratio χ provides a simplifying notion of a geometrical parameter. In our experiments, the Archimedes number, determined by the fluid properties, bands size and density, is on the order to 95000. We additionally estimate the translational Reynolds number ($\mathrm{Re} = v_z\rho R/\mu$) and the signed rotational Reynolds number ($\mathrm{Re}_r = \omega_{cm}\rho R^2/\mu$) to provide a quantitative indication of the inertial regime of the bands during sedimentation. We must highlight that Re varies with χ, as its value for any given band depends on its terminal velocity, which is determined by the equilibrium between the gravitational forces and the drag forces. Thus, in presenting our findings, for each family of bands we use the translational Reynolds number relative to the Reynolds number of the bands with highest aspect ratio $\mathrm{Re}/\mathrm{Re}_{max}$. This to indicate the relative velocity of a band with respect to the maximum velocity observed for a family of bands. Additionally, we use the ratio $\mathrm{Re}_r/\mathrm{Re}$ of the rotational to translational Reynolds numbers, to indicate the coupling between the translational and angular velocity of the bands. $\mathrm{Re}/\mathrm{Re}_{max}$ and $\mathrm{Re}_r/\mathrm{Re}$ allow us to track relative variations for each band, as well as comparing those variations with the simulation results.

III. RESULTS AND DISCUSSION

A. Sedimentation of Möbius bands

Prior research on screwlike objects has demonstrated that their sedimenting behavior varies with orientation [23], resulting in helical trajectories and orbits of various types. However, in our research on triply twisted, threefold symmetric Möbius bands, we found that their behavior showed no significant dependence on initial orientation. Our observations reveal that these bands align almost horizontally regardless of their starting position, suggesting a preferred orientation during sedimentation [35]. For values of $\chi > 0.6$, tumbling motion can induce periodic variations in the alignment of the bands. However, their orientation always varies around the x-y plane (see Fig. 2). For relatively small values of χ, the tumbling disappear and each band considered showed a unique preferential horizontal orientation. Such behavior is in line with the presence of a stable dominant mode in the translational response of the bands. Similar horizontal stabilization has been observed in the dynamics of rigid [20] and flexible [21] knotted loops.

In our experimental observations, bands of type R achieved Reynolds numbers within the range $250 \leqslant \mathrm{Re} \leqslant 300$, owing to their relatively higher terminal velocities. In contrast, bands of types D and B achieved Reynolds numbers in the lower range of $50 \leqslant \mathrm{Re} \leqslant 250$ due to their comparatively lower terminal velocities. Supporting videos show the sedimentation of sample bands of each type with various aspect ratios. Notably, bands of type D exhibited more pronounced tumbling compared to bands of type B and R. However, the variations in the tumbling angle Ψ decreases as the angle α between the cylinders used for constructing the bands increases. Increasing α yields wider inner channels, stabilizing the flow within the folds of the bands. It is important to highlight that triply twisted bands possess an additional characteristic dimension associated with their vein (or internal opening). Bands of type D have narrower spaces between folds in comparison to bands of type R and B, resulting in higher shear rates interior to their undulations. Consequently, inertial instabilities are responsible for the pronounced tumbling motion as bands of type D sediment [1]. Unlike bands of type D, bands of type R exhibit more stable rotation during sedimentation, with tumbling observed as χ approaches unity. We hypothesize the petal-like structures of bands of type R offer greater resistance than other types of bands in this study, contributing to their stable rotation.

We consistently observe rotational motion during the sedimentation of each family of chiral bands. Specifically, each band of type D spins in the direction opposite to its twist

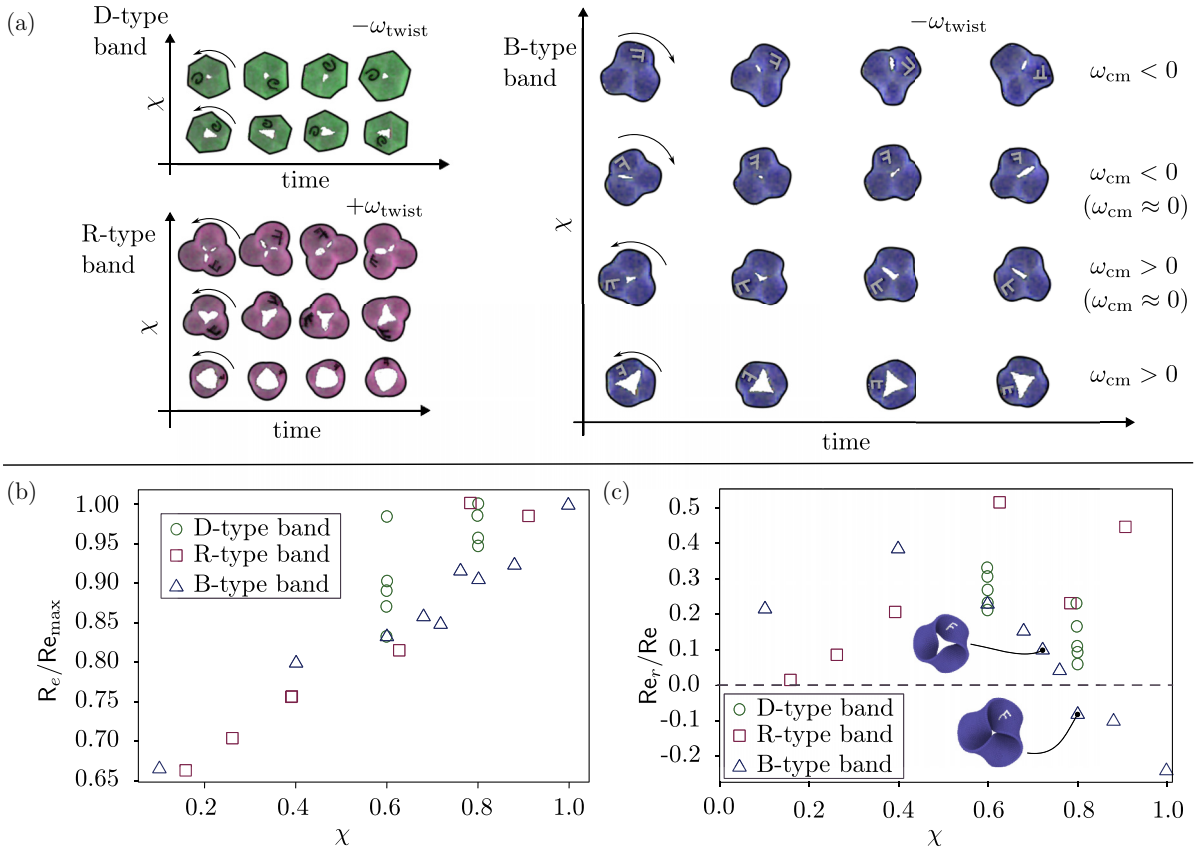

FIG. 3. Experimental data on the sedimentation of triply twisted Möbius bands. (a) Mirrored-bottom images at equally spaced time intervals of D (developable), R (rotoidal), and B (binomial scroll) type Möbius bands during sedimentation, and for various aspect ratios χ. χ is defined as the ratio w/w_{max} where w is the band's width, and w_{max} is the maximum band's width before self-intersection. The arrows indicate the direction of rotation. The spinning direction in mirrored-bottom view coincides with the spinning from the top view. Bands of type D and B constructed with negative twist (ω_{twist}), whereas bands of type R positive. (b) Ratio of translational Reynold number Re to maximum translational Reynold number Re_{max} as a function of χ for bands of type D (circles), R (squares), and B (triangles). The Re_{max} is the Reynold number at $\chi = 1$. (c) Ratio of rotational Reynolds number Re_r to Re for bands of type D, R, and B. The colors of the bands were edited to coincide with the colors in Fig. 1, and the markers on the bands are color enhanced to facilitate their visualization.

orientation [$\text{sgn}(\text{spin}) = -\text{sgn}(\omega_{\text{twist}})$]. Conversely, each band of type R spins in the same direction as its twist [$\text{sgn}(\omega_{\text{cm}}) = \text{sgn}(\omega_{\text{twist}})$] To illustrate the different spinning directions between bands of type D and R, we present experimental results in Fig. 3(a). In the case of bands of type D, those with negative twists undergo a counterclockwise spinning, while bands of type R, which have a positive twist, exhibit positive rotational direction. Bands of type B, which have a negative twist, exhibit two different spinning directions (from counterclockwise to clockwise), or a chiral-response switch, as their aspect ratio increases. Snapshots of B bands with negative twists and representative choices of χ are provided in Fig. 3(a). Videos comprising the snapshots in Fig. 3 are provided as Supplemental Material [34]. The chiral transition occurs within a narrow window of χ values, and implies the existence of a critical value $\chi_{\text{crit}} \approx 0.8$ where spinning is nearly suppressed ($\omega_{\text{cm}} \approxeq 0$). At $\chi = \chi_{\text{crit}}$, energy dissipation is primarily linked to predominantly vertical translation and possible vortex formation. In Figs. 3(b) and 3(c), we present the impact of the parameter χ on the ratios $\text{Re}/\text{Re}_{\text{max}}$ and Re_r/Re for the different types of bands. Notably, bands of type R show a nearly monotonic increase in the ratio $\text{Re}/\text{Re}_{\text{max}}$, while bands of type B exhibit a transition where the ratio experiment a large increase, from approximately 0.8–1, between $0.7 < \chi < 0.9$, that coincide with the value of χ for the chiral-response switch. Overall, bands of type B behave like bands of type R for $\chi \geqslant \chi_{\text{crit}}$, while resembling bands of type D for $\chi \leqslant \chi_{\text{crit}}$.

The dynamics of triply twisted Möbius bands are similar to those observed in rigid and flexible knotted loops [20,21], that possess equivalent chirality and nonorientability features. Like the Möbius bands considered in the present work, sedimenting knotted loops exhibit preferential alignment and spinning rotation correlated with the handedness of the knot. The remarkable difference observed for bands of type B is the existence of two distinct rotational modes for bands with the same handedness. A transition in chiral response akin to that observed in bands of type B has also been documented for superhelical structures [36]. A superhelix is composed of a helix with a short pitch configured along an axis that itself forms a helix of the opposite handedness but larger pitch, referred to as the axial helix. In such composite structures, the directional rotations of each helical component are in conflict. If the amplitude or wave number of the axial helix is minimal,

the dynamics of the superhelix are predominantly influenced by the handedness of the component with the shorter pitch. Conversely, at larger amplitudes or wave numbers, the rotational behavior of the superhelix aligns with the handedness of the axial helix. Notably, superhelices exhibit a crossover in their dynamical response at a specific amplitude and wave number threshold, at which the structure ceases to rotate [36]. This phenomenon closely resembles our discovery of a critical aspect ratio for bands of type B. Beyond this ratio, not only do such bands stop rotating, but there is also a reversal in the direction in which they rotate.

To simulate the sedimentation behavior of the bands, we use dissipative particle dynamics (DPD) [37,38]. Computationally, the angular velocity of the simulated bands is computed from the evolution of the eigenvector associated with the largest eigenvalue of the gyration tensor. A detailed description of the DPD methodology is provided in the Appendix B. Simulation studies validate the presence of a chiral transition for bands of type B (see videos in Supplemental Material [34]), in agreement with our experimental findings. The simulation results also validate axial alignment and spinning direction in bands of this type, as illustrated in Fig. 4(a). However, it is noteworthy that the critical aspect ratio at which the chiral transition occurs shifts to $\chi \approx 0.68$ in simulations from $\chi \approx 0.78$ in experiments [see Fig. 4(b)]. It is important to acknowledge that DPD simulations provide a qualitative description of the dynamics of the bands in a fluid regime that is closer to the regime of our experimental conditions. However, certain effects observed in the experiments, such as tumbling, as well as the discrepancy in Reynolds numbers between bands of type R and B, are not fully replicated in the computational test. The Reynolds number in the experiments ranged from 50–400, whereas for DPD the Reynolds number ranged from 5–25. These discrepancies arise due to inherent limitations of DPD in explicitly enforcing no-slip boundary conditions and in accounting for effects associated with Schmidt number variations. Although the numerical model has limitations, it still manages to replicate the chiral response and its transition observed in experiments. This underscores the dominant influence of shape-related characteristics on sedimentation dynamics, even in the presence of substantial inertial effects.

For simple objects, such as spheres [39], it has been previously observed that instabilities and wake formation can readily occur in the range of Reynolds numbers ($50 \leqslant \mathrm{Re} \leqslant 400$) that we considered. Therefore, for chiral particles, the emergence of instabilities may have an important effect due to complex interactions between the fluid and the structural features of the particle [25]. It has been noted that a chiral object can display asymmetric bistability in its orientation, with the orientation determined by the flow conditions. To enhance our understanding of the impact of the chiral switch exhibited by bands of type B on the fluid, a series of experiments were conducted by initially coating the bands with a fluorescein-salt solution, allowing for the visualization of the fluid flow induced by the sedimenting bands. It is important to emphasize that a comprehensive understanding of fluid-induced drag would require experimental consideration of the scale of wake structures. This would include examining aspects such as the circulation, magnitude of vorticity, and momentum deficit.

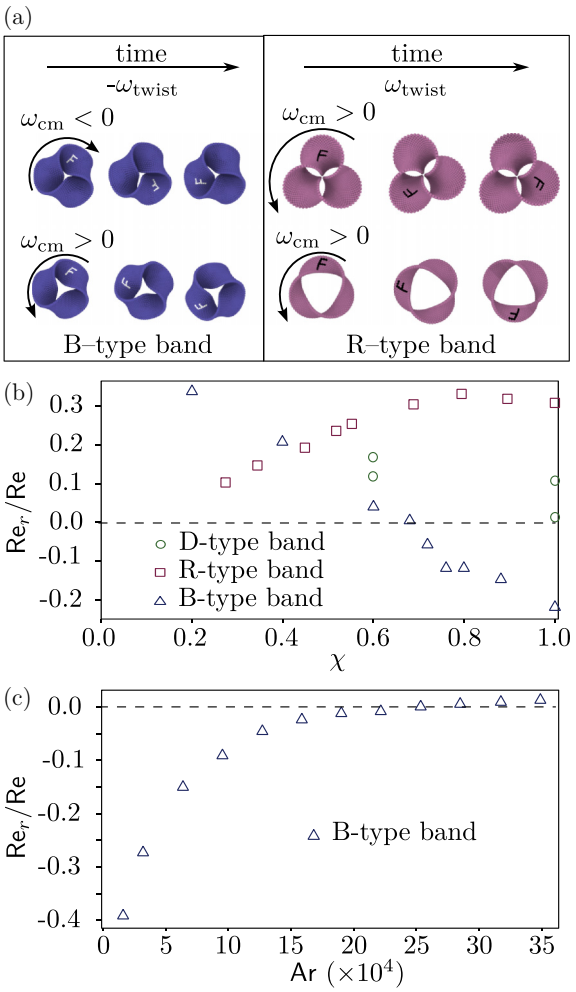

FIG. 4. Simulation data on the sedimentation of triply twisted Möbius bands. (a) Top-view images of bands of types B and R during sedimentation at equally spaced time intervals, and for two representative values of the ratio $\chi = w/w_{\mathrm{max}}$, where w represents the width of a band and w_{max} is the maximum value of w that can be achieved without self-intersection. (b) Ratio of the rotational Reynolds number Re_r to the translational Reynold number Re as a function of the aspect ratio χ. (c) $\mathrm{Re}_r/\mathrm{Re}$ as a function of the Archimedes number Ar for a constant value of $\chi = 0.68$.

However, conducting such in-depth analyses falls outside the purview of our current investigation. In Fig. 5, we present the lateral and bottom views of two sedimenting bands of type B with different aspect ratio, $\chi < \chi_{\mathrm{crit}}$ and $\chi > \chi_{\mathrm{crit}}$ (see also videos in SM [34]). For clarity, the lateral images have been filtered and color enhanced. Notably, the wakes generated by the bands with $\chi = 0.74$ and $\chi = 0.78$ exhibit a different shape. The relative size of the wake is highlighted with blue solid lines in Fig. 5. Specifically, the wake width produced by the band at $\chi = 0.78$ is more compact ($\approx 5R$) in comparison to that generated at $\chi = 0.74$ ($\approx 7R$). This observation indicates that at $\chi = 0.78$, the band causes less disruption to the fluid, whereas a modest change in the aspect ratio to $\chi = 0.74$ results in significant energy dissipation and vorticity generation in the wake. Overall, even a minor change in the aspect ratio of the band seems sufficient to induce modifications in the

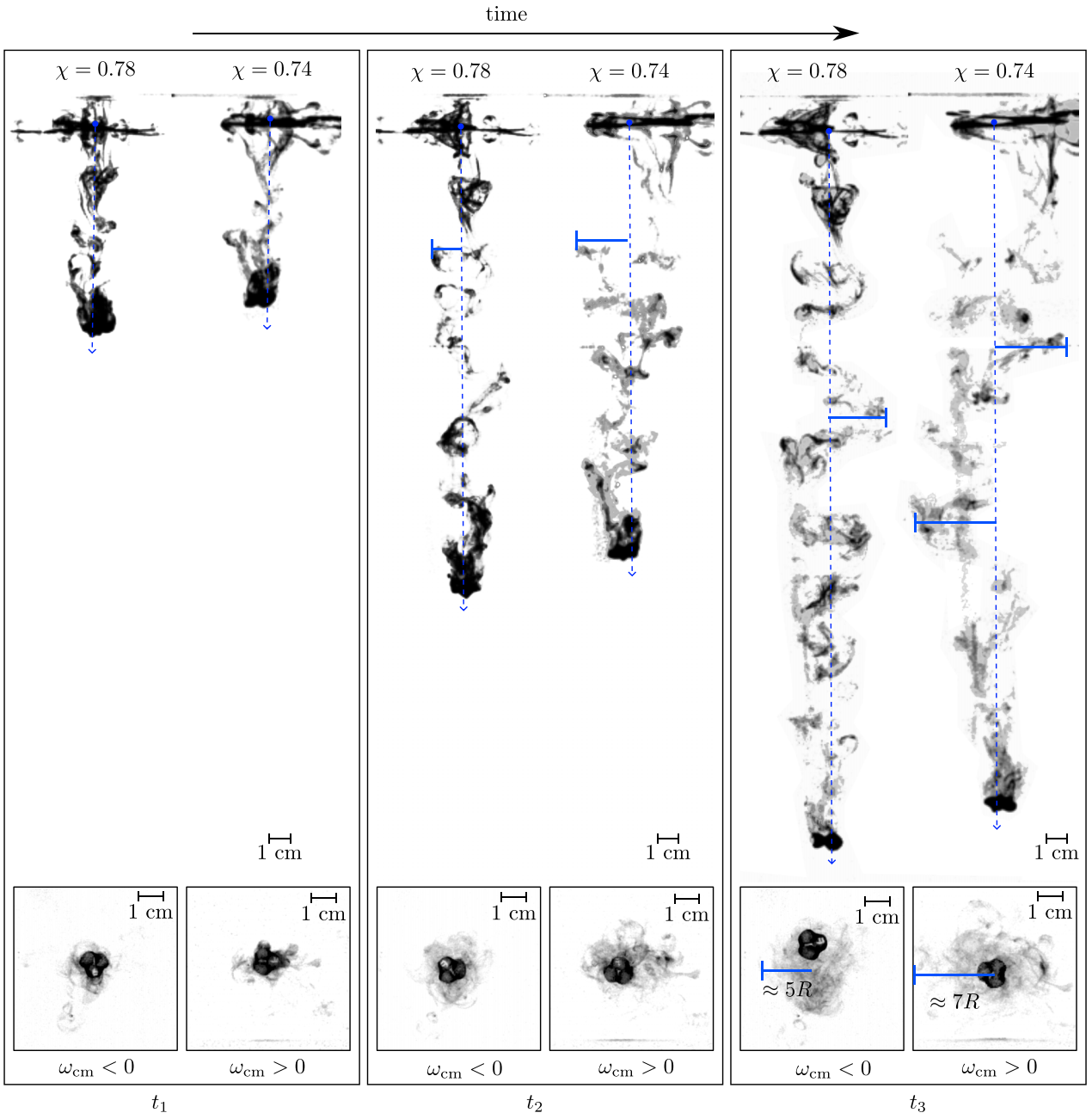

FIG. 5. Sedimentation of fluorescein-tinted triply twisted Möbius bands in water. Side view of the sedimentation of bands of type B with aspect ratio $\chi = 0.78$ and $\chi = 0.74$, which exhibit negative and positive angular speed (ω_{cm}), respectively, and for increasing instants t_1, t_2, and t_3 of time. χ is defined as w/w_{max} where w is the band width and w_{max} is the maximum band width before self-intersection. Inside images correspond to mirrored-bottom view of the same Möbius bands at times t_1, t_2, and t_3. The wake created by the bands spans over a distance several times larger than the projected radius R. Blue-solid lines indicate the maximum size of the wake. The original images were taken with a black background to enhance the contrast with the green fluorescein. Postprocessing of the images was necessary to obtain a white background with gray scale wake.

fluid-induced drag, which, combined with inertial effects, can drive changes in the chiral response of a sedimenting band of type B.

B. Hydrodynamic resistance tensor

Generally, the hydrodynamic resistance tensor of an object depends on its geometry. However, objects with similar geometrical features need not have identical hydrodynamic resistance tensors [29]. Thus, despite the common symmetrical features of the triply twisted bands investigated, variations in the hydrodynamic resistance can serve as an indicator of the chiral switch observed for bands of type B. To further elucidate whether the chiral switch for bands of type B can be readily identified based on changes in their hydrodynamic drag, we use the rigid multiblob methodology [40] to calculate the resistance tensor $\mathbb{R}$ for all three types of bands with various aspect ratios at $\mathrm{Re} \approx 0$. Determination of the

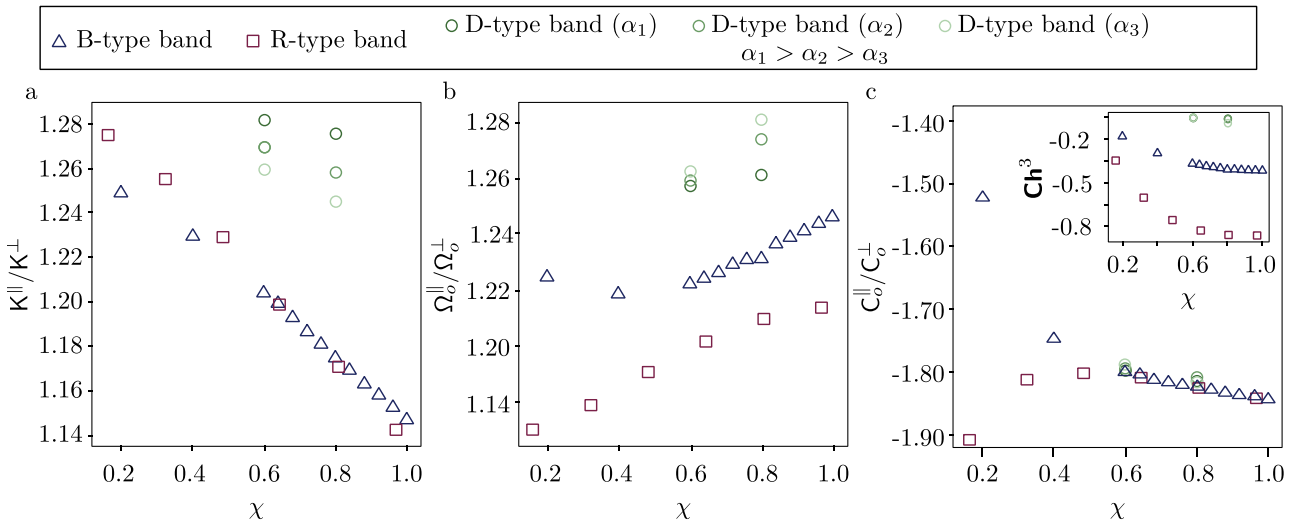

FIG. 6. Variation of the components in the resistance tensor $\mathbb{R}$ with respect to the aspect ratio χ of the bands. Ratio of: (a) translational tensor components parallel $\mathsf{K}^{\parallel}$ to perpendicular $\mathsf{K}_{\perp}$, (b) rotational tensor components parallel $\Omega_o^{\parallel}$ to perpendicular $\Omega_o^{\perp}$, and *c) coupling tensor components parallel $\mathsf{C}_o^{\parallel}$ to perpendicular $\mathsf{C}_o^{\perp}$ as a function of χ. The components are parallel or perpendicular to the gravitational force.

resistance tensor offers a direct way to identify intrinsic chirality [17]. Without loss of generality, we present results for bands with negative chirality. For the computations, we take the centroid of the band to be located at the origin o of an orthonormal basis, $\{\boldsymbol{e}_x, \boldsymbol{e}_y, \boldsymbol{e}_z\}$, chosen such that $\boldsymbol{e}_z$ is parallel to the vector of the gravitational force (and the axis of rotation). In Figs. 6(a)–6(c), we present the components of the translational, rotational, and coupling dyads $\mathbf{K}$, $\boldsymbol{\Omega}_o$, and $\mathbf{C}_o$, respectively, as a function of χ. To highlight disparities in the computed values of the drag along different directions axis, we used the ratio of the components $\mathbf{K}$, $\boldsymbol{\Omega}_o$, and $\mathbf{C}_o$ parallel ($\parallel$) and perpendicular ($\perp$) to $\boldsymbol{e}_z$. For instance, for the translational tensor, $\mathsf{K}^{\parallel} = \boldsymbol{e}_z \cdot \mathbf{K} \cdot \boldsymbol{e}_z$, whereas $\mathsf{K}^{\perp} = \boldsymbol{e}_x \cdot \mathbf{K} \cdot \boldsymbol{e}_x$. Notably, the ratio $\mathsf{K}^{\parallel}/\mathsf{K}^{\perp}$ exhibits a monotonic decrease for bands of type B and R as χ increases, while the rotational ratio $\Omega_o^{\parallel}/\Omega_o^{\perp}$ shows a moderate variation with mean values of approximately 1.23 for bands of type B and at approximately 1.26 for bands of type D. Overall, for large values of χ, bands of type B and R exhibit similar hydrodynamic resistance. Figure 6(c) provides deeper insight into the behavior of triply twisted bands. The opposite sign in the components that characterize the coupling resistance ($\mathsf{C}_o^{\parallel}/\mathsf{C}_o^{\perp} < 0$) indicate that the chirality in the parallel and perpendicular directions are different. For chiral bodies, the mobility matrix $\mathbb{M} = \mathbb{R}^{-1}$ characterizes the direction in which that body rotates through the chirality matrix $\mathbf{Ch} = \mathcal{C}/(\chi\mathcal{R})$ [27,28] where $\mathcal{C}$ and $\mathcal{R}$ are the coupling and rotation dyads of the mobility matrix $\mathbb{M}$, respectively. Granted that $\mathbf{Ch}$ is expressed relative to a basis $\{\boldsymbol{e}_1, \boldsymbol{e}_2, \boldsymbol{e}_3\}$ defined by the eigenvectors of $\mathcal{R}$, with corresponding eigenvalues enumerated in ascending order, $\mathcal{R}^1 \leqslant \mathcal{R}^2 \leqslant \mathcal{R}^3$, the diagonal elements of $\mathbf{Ch}$ are expressed as $\mathbf{Ch}^i = \mathcal{C}^{ii}/(\chi\mathcal{R}^i)$, $i = 1, 2, 3$. The inset plot in Fig. 6(c) present the values of $\mathbf{Ch}^3$ as a function of χ for each family of bands. In general, $\mathbf{Ch}$ monotonically decreases as χ increases and does not evidence the characteristic transition observed experimentally. Among the three types of bands considered, the eigenvalues of $\mathbf{Ch}$ have the largest magnitudes for bands of type R and the smallest magnitudes for bands of the type D. For bands of type B, the eigenvalues of $\mathbf{Ch}$ fall in between those of types R and D, suggesting a hydrodynamic response that is likely a transitional state between the pronounced characteristics of bands of type R and the subdued features of bands of type D. Despite the insights provided by the resistance tensor $\mathbb{R}$ at low Reynolds numbers, accurately discerning the observed chiral response for bands of type B poses a formidable challenge. The transition between the two distinct spinning directions exhibited by bands of type B is influenced by multiple factors, such as the balances of forces and moments, the alignment of the band, and the onset of inertial instabilities. These complexities highlight the need for further investigations and a comprehensive understanding of the underlying dynamics.

A partial explanation for the observed chiral-response transition for bands type B might be linked to their construction method; these bands are obtained by isometrically deforming a helicoid. Previous studies have shown that spirals do not spin the same way if they are not spinning around their central spiral axis [29]. As the rotation of a band of type B during sedimentation occurs along a rotation axis that does not align locally with the bent image of the helicoidal axis (axis along which an helicoid is constructed), the influence of off-helicoidal-axis rotation might be sensitive to the aspect ratio of the band.

As the transition in chiral response for bands of type B is influenced not only by the band's characteristic size χ but also by alterations in the flow regime, we explore deeper into this phenomenon through additional numerical DPD investigations. For this purpose, we focus on bands of type B with positive twist near the critical aspect ratio, $\chi = 0.68$ [prior to the chiral switch in our DPD model $\mathrm{sgn}(\mathrm{spin}) = -\mathrm{sgn}(\omega_{\mathrm{twist}})$], and manipulate the values of Ar by adding an external force applied to the band [see Fig. 4(c)]. We observe that for this constant value of χ, the band present a chiral transition at $\mathrm{Ar} \approx 250\,000$, suggesting the existence of a chiral

transition for different aspect ratios of bands of type B as the Ar number changes.

IV. CONCLUSIONS AND OUTLOOK

Our study challenges a generally accepted concept for the sedimentation of chiral objects—namely, the chirality of an object determines its spinning direction during sedimentation. Specifically, despite sharing identical topology and intrinsic chirality, triply twisted Möbius bands with threefold rotational symmetry can exhibit divergent chiral responses attributed to their unique curvatures. Our exploration of bands of type binormal scroll (bands of type B) uncovers a nuanced interplay of torques and forces that evolve with changing aspect ratios, modulated by the influence of inertial effects. This intricate relationship results in a distinctive transition in the spinning direction of the band; a phenomenon absent in other triply twisted bands. Computational simulations robustly confirm these experimental insights, further elucidating the intricate interdependence between gravitational and viscous forces and the critical aspect ratio dictating the transition.

We hypothesize that the chiral transition observed for bands of type B stems from its geometrical properties resembling superhelices. This resemblance arises from its construction, which starts from helicoids that are isometrically deformed to form the bands. The way bands of type B rotate during sedimentation—specifically, around a symmetry axis that generally differs from the original helicoidal axis—could indicate a reduction in their chiral response. Furthermore, the sudden change in the response of the bands, similar to reaching a critical aspect ratio, is consistent with phenomena seen in superhelical structures. This similarity hints at the existence of two conflicting chiral forces within bands of type B.

Our finding that the spinning direction of bands with a given chirality depends on the aspect ratio suggests broader implications. These results signal promising prospects in designing responsive materials and microswimmers without self-propulsion, harnessing the potential for hydrodynamically driven chiral-response switching. This opens avenues for creating deployable objects such as responsive materials and microswimmers, capable of dynamic rotational responses. It also invites exploration into analogous entities possessing comparable attributes. Additionally, it introduces the intriguing concept of hydrodynamically responsive chirality in objects featuring nonzero coupling tensors. Furthermore, our study underscores the limitations of relying solely on intrinsic chirality to characterize the dynamics of chiral particles in fluids, especially in the presence of inertial instabilities. This highlights the necessity for further exploration into the intricate network of emergent hydrodynamic interactions.

In closing, our study contributes novel insights to the captivating domain of chiral hydrodynamics, blending fundamental understanding with tangible applications. By providing new insights into the hydrodynamic intricacies of chiral objects, our work can pave the way for innovative technologies and devices endowed with unique attributes. As the scientific narrative of chiral hydrodynamics continues to evolve, our findings are poised to stimulate further discoveries, facilitate groundbreaking applications, and enrich our grasp of intricate fluid dynamics.

ACKNOWLEDGMENTS

This work was supported by the Okinawa Institute of Science and Technology Graduate University with subsidy funding from the Cabinet Office, Government of Japan. N.M. acknowledges the support from the European Union's Horizon 2020 under the Marie Sklodowska-Curie Individual Fellowships Grant No. 101021893, with acronym ViBRheo.

APPENDIX A: EXPERIMENTAL SEDIMENTATION

To conduct our sedimentation studies, we utilized polystyrene bands with a density of $1.17\,\mathrm{g/cm^3}$ in water at room temperature. These bands were 3D printed using the OBJET 500 from STRATASYS company, and were placed in a container with dimensions of $0.20 \times 0.20 \times 0.60\ \mathrm{m^3}$. To identify the direction of the spin, the bands were marked with the letter F or G. We used two cameras, an Ultrahigh-Speed Camera (v2512) and a High-speed camera (Phantom Miro LC-120), to record the falling of the objects at a rate of 100 frames per second. The cameras were equipped with Nikon AFS 60 mm f/2.8G and Sigma 24-70 mm f2.8 lenses and were positioned two meters away from the sedimentation container. The cameras were aligned to capture 0.4 m of the vertical trajectory, while three different markers were placed in the sedimentation container at 10 cm, 25 cm, and 40 cm from the bottom to facilitate trajectory analysis. To record the rotation of the bands, we placed a tilted mirror at the bottom of the container with an angle of 45°. The marks (F or G) in sedimenting bands pointed in the sedimentation direction for observation through the mirror, and their spinning direction coincides with top-view observation. The vertical distortion from the center of the field of view up to the edges was ± 1.5 cm, while the horizontal distortion was $\leqslant 0.4$ cm. The 3D-printed bands were constructed with a positive twist, resulting in a positive spin of their intrinsic chirality. The width of the band was varied in different experiments to investigate the effect of the aspect ratio, while their projected radius and thickness were kept constant at 10 mm and 0.8 mm, respectively. The Reynolds numbers evaluated ranged from 50–350. To extract the position of the bands from the recorded images, we used the distribution of the pixels to track the position of the center of mass of the band in each camera and constructed the three-dimensional trajectories.

To extract the linear and angular velocity of the bands we analysed the images obtained every 60 frames per second. Each image was divided into two regions to recover the lateral and bottom view reflected in the mirror. The image segmentation was then conducted in each of the projections to retrieve the band's pixel count and distribution. Trajectories were reconstructed from the position of the mean distribution of the pixels at each frame. We used the letter marker on the bands to estimate their angular velocity around the vertical axis of a reference frame with the origin at the center of mass of the band.

APPENDIX B: DISSIPATIVE PARTICLE DYNAMICS SEDIMENTATION SIMULATIONS

We modeled the sedimentation of the bands using the dissipative particle dynamics method (DPD) [37]. DPD is

a particle-based method that consistently captures hydrodynamic effects, and has been widely used to study soft matter in different fields [41,42]. In DPD, we discretized the triply twisted bands using a single layer of N_p soft beads rigidly connected, whereas the fluid is discretized using individually interacting particles. A sketch of the discretized version of the different type of bands is presented in SM [34], Fig. 4. See also SM [34], for the point coordinates of the discretized bands. During the simulations, the force between the fluid and the beads of the bands was computed, and the position and velocity of the center of mass of the band were updated due to the net force acting on it. The position of the N_p beads of the bands was updated following the rigid-body dynamics. To conduct these simulations we used the DPD distribution implemented in LAMMPS [43], as well as the rigid-body motion setting available there. For a detailed description of the DPD method the reader is referred to SM [34]. The visualization of the DPD simulation results was done using the software OVITO [44].

Sedimentation simulations were conducted in elongated boxes with sizes $L_x = 12R$, $L_y = 12R$, and $L_z = 180R$. All the simulations used periodic boundary conditions on the x and y axis, whereas reflecting walls are used on the z axis. The size L_x and L_y were defined to avoid the effects of the periodic boundary condition. The center of mass X_O of bands was initially located at the top of the box at $[0.5L_x, 0.5L_y, 0.9L_z]$. The bands were subjected to an external force f_g on the $-z$ direction. Due to the nonperiodicity in z, the results of the simulations were analyzed using trajectories in the range $0.8L_z > X_O > 0.1L_z$, to neglect wall effects.

The interaction parameter of the DPD conservative potential was set as $a_{bb} = a_{ff} = 25.0$, where bb and ff correspond to interactions between band-band and fluid-fluid beads, respectively. The interaction parameter between band and fluid beads (bf) was set as $a_{bf} = 65.0$ to ensured no-penetration boundary condition at the surface of the bands. Additionally, the distance between the beads forming the bands was $0.75r_c < r_{bb} < r_c$, where r_c is the DPD cutoff radius. These values ensure the control of the density fluctuations across the box and satisfactorily avoid the passing of fluid particles across the band's domains. Additionally, to minimize resolution effects due to the relative size between the band and the discrete size of the fluid, all the bands were constructed such that the width w of the band has to be larger than $5r_c$, and the band radius $R > 10r_c$. Nonslip boundary conditions were not explicitly accounted for using the standard DPD methodology, therefore, the simulations cannot be considered strictly no-slip or slip. Simulations were conducted at $k_BT = 1$, $m = 1$, $r_c = 1$, $\rho_n = 3$. At the fluid conditions used in our simulations, the viscosity of DPD can be approximated as 0.866 in reduced units [45].

APPENDIX C: RESISTANCE TENSOR CALCULATION

We used the rigid multiblob (RMB) methodology [40] to estimate numerically the resistance tensor $\mathbb{R}$ for the different bands at zero Reynolds number. RMB has been successfully applied to study the hydrodynamic behavior of rigid objects with complex morphologies [46,47]. In the RMB approach, only the set of N_p beads was considered, whereas hydrodynamic interactions with the solvent were accounted for analytically. To compute $\mathbb{R}$, we used the discretization adopted for the DPD simulations. However, the beads were treated as rigid bodies (instead of the soft DPD beads), with a hydrodynamic radius $r_{RMB} = r_{bb}/2$. The hydrodynamic interactions between beads were represented using the generalized Rotne-Prager-Yamakawa tensor for an unbounded region [40,48]. For further details concerning the implementation of the RMB, the reader is referred to Ref. [40].

[1] P. Ern, F. Risso, D. Fabre, and J. Magnaudet, Wake-induced oscillatory paths of bodies freely rising or falling in fluids, Annu. Rev. **44**, 97 (2012).

[2] Z. J. Wang, Dissecting insect flight, Annu. Rev. Fluid Mech. **37**, 183 (2005).

[3] D. Lentink, W. B. Dickson, J. L. Van Leeuwen, and M. H. Dickinson, Leading-edge vortices elevate lift of autorotating plant seeds, Science **324**, 1438 (2009).

[4] P. Kry and R. List, Angular motions of freely falling spheroidal hailstone models, Phys. Fluids **17**, 1093 (1974).

[5] G. Yang, Z. Yu, X. Peng, Y. Zhou, A. B. M. Baki, and W. Zhang, Settling behaviors of microplastic disks in acceleration fall, Mar. Pollut. Bull. **202**, 116296 (2024).

[6] Z. Geng, B. Xiong, L. Wang, K. Wang, M. Ren, L. Zhang, J. Zhu, and Z. Yang, Moebius strips of chiral block copolymers, Nature Commun. **10**, 4090 (2019).

[7] G. Ouyang, L. Ji, Y. Jiang, F. Würthner, and M. Liu, Self-assembled Möbius strips with controlled helicity, Nature Commun. **11**, 1 (2020).

[8] X. Shi, A. K. Pumm, J. Isensee, W. Zhao, D. Verschueren, A. Martin-Gonzalez, R. Golestanian, H. Dietz, and C. Dekker, Sustained unidirectional rotation of a self-organized DNA rotor on a nanopore, Nature Phys. **18**, 1105 (2022).

[9] L. Zhang, T. Wang, Z. Shen, and M. Liu, Chiral nanoarchitectonics: Towards the design, self-assembly, and function of nanoscale chiral twists and helices, Adv. Mater. **28**, 1044 (2016).

[10] W. Fan, T. M. Fukunaga, S. Wu, Y. Han, Q. Zhou, J. Wang, Z. Li, X. Hou, H. Wei, Y. Ni, H. Isobe, and J. Wu, Synthesis and chiral resolution of a triply twisted Möbius carbon nanobelt, Nature Synth. (2023).

[11] S. Yoo and Q. Park, Metamaterials and chiral sensing: A review of fundamentals and applications, Nanophoton. **8**, 249 (2019).

[12] H. Zhang, S. Li, A. Qu, C. Hao, M. Sun, C. Xu, and H. Kuang, Engineering of chiral nanomaterials for biomimetic catalysis, Chem. Sci. **11**, 12937 (2020).

[13] Y.-J. Kim and W. J. Rae, Separation of screw-sensed particles in a homogeneous shear field, Int. J. Multiphase Flow **17**, 717 (1991).

[14] S. Meinhardt, J. Smiatek, R. Eichhorn, and F. Schmid, Separation of chiral particles in micro- or nanofluidic channels, Phys. Rev. Lett. **108**, 214504 (2012).

[15] T. M. Hermans, K. J. M. Bishop, P. S. Stewart, S. H. Davis, and B. A. Grzybowski, Vortex flows impart chirality-specific lift forces, Nature Commun. **6**, 5640 (2015).

[16] J. B. Clemens, O. Kibar, and M. Chachisvilis, A molecular propeller effect for chiral separation and analysis, Nature Commun. **6**, 7868 (2015).

[17] M. Doi and M. Makino, Separation of chiral particles in a rotating electric field, Phys. Fluids **28**, 093302 (2016).

[18] M. Makino and M. Doi, Migration of twisted ribbon-like particles in simple shear flow, Phys. Fluids **17**, 103605 (2005).

[19] T. A. Witten and H. Diamant, A review of shaped colloidal particles in fluids: Anisotropy and chirality, Rep. Prog. Phys. **83**, 116601 (2020).

[20] C. Weber, M. Carlen, G. Dietler, E. J. Rawdon, and A. Stasiak, Sedimentation of macroscopic rigid knots and its relation to gel electrophoretic mobility of DNA knots, Sci. Rep. **3**, 1091 (2018).

[21] M. Gruziel, K. Thyagarajan, G. Dietler, A. Stasiak, M. L. Ekiel-Jeżewska, and P. Szymczak, Periodic motion of sedimenting flexible knots, Phys. Rev. Lett. **121**, 127801 (2018).

[22] M. Gruziel-Słomka, P. Kondratiuk, P. Szymczak, and M. L. Ekiel-Jezewska, Stokesian dynamics of sedimenting elastic rings, Soft Matter **15**, 7262 (2019).

[23] M. Palusa, J. de Graaf, A. Brown, and A. Morozov, Sedimentation of a rigid helix in viscous media, Phys. Rev. Fluids **3**, 124301 (2018).

[24] N. W. Krapf, T. A. Witten, and N. C. Keim, Chiral sedimentation of extended objects in viscous media, Phys. Rev. E **79**, 056307 (2009).

[25] A. Zöttl, F. Tesser, D. Matsunagae, J. Laurenta, O. du Roure, and A. Lindner, Asymmetric bistability of chiral particle orientation in viscous shear flows, Proc. Natl. Acad. Sci. USA **120**, 45 (2023).

[26] J. Happel and H. Brenner, *Low Reynolds Number Hydrodynamics*, Volume 1 of Mechanics of Fluids and Transport Processes (Springer, Dordrecht, 1981).

[27] K. I. Morozov, Y. Mirzae, O. Kenneth, and A. M. Leshansky, Dynamics of arbitrary shaped propellers driven by a rotating magnetic field, Phys. Rev. Fluids **2**, 044202 (2017).

[28] Y. Mirzae, O. Dubrovski, O. Kenneth, K. I. Morozov, and A. M. Leshansky, Geometric constraints and optimization in externally driven propulsion, Sci. Robot. **3**, eaas8713 (2018).

[29] M. P. Dalwadi, C. Moreau, E. A. Gaffney, B. J. Walker, and K. Ishimoto, Generalised Jeffery's equations for rapidly spinning particles. Part 2. Helicoidal objects with chirality, J. Fluid Mech. **979**, A2 (2024).

[30] J. Schönke, M. Grunwald, and E. Fried, Construction of unknotted and knotted symmetric developable bands, Symmetry **13**, 431 (2021).

[31] J. H. Piette, N. Moreno, E. Fried, and A. F. Giacomin, The complex viscosity of Möbius macromolecules, Phys. Fluids **32**, 093107 (2020).

[32] J. Schönke and E. Fried, Single degree of freedom everting ring linkages with nonorientable topology, Proc. Natl. Acad. Sci. USA **116**, 90 (2019).

[33] V. Chaurasia and E. Fried, Stable Möbius bands from isometrically deformed circular helicoids, J. Elast. **155**, 601 (2023).

[34] See Supplemental Material at http://link.aps.org/supplemental/10.1103/PhysRevResearch.6.033141 for description of the computational method, additional S. Figures and sedimentation Videos. STL files of the printed bands and data points of the discretized bands.

[35] B. Moths and T. A. Witten, Full alignment of colloidal objects by programed forcing, Phys. Rev. Lett. **110**, 028301 (2013).

[36] S. Jung, K. Mareck, L. Fauci, and M. J. Shelley, Rotational dynamics of a superhelix towed in a Stokes fluid, Phys. Fluids **19**, 103105 (2007).

[37] R. D. Groot and P. B. Warren, Dissipative particle dynamics: Bridging the gap between atomistic and mesoscopic simulation, J. Chem. Phys. **107**, 4423 (1997).

[38] N. Moreno, S. P. Nunes, and V. Calo, Consistent model reduction of polymer chains in solution in dissipative particle dynamics: Model description, Comput. Phys. Commun. **196**, 255 (2015).

[39] T. A. Johnson and V. C. Patel, Flow past a sphere up to a Reynolds number of 300, J. Fluid Mech. **378**, 19 (1999).

[40] F. B. Usabiaga, B. Kallemov, B. Delmotte, A. P. S. Bhalla, B. E. Griffith, and A. Donev, Hydrodynamics of suspensions of passive and active rigid particles: A rigid multiblob approach, Commun. Appl. Math. Comput. Sci. **11**, 217 (2016).

[41] N. Moreno, B. Sutisna, and E. Fried, Entropic factors and structural motifs of triblock-terpolymer-based patchy nanoparticles, Nanoscale **12**, 22059 (2020).

[42] N. Moreno, P. Vignal, J. Li, and V. Calo, Multiscale modeling of blood flow: Coupling finite elements with smoothed dissipative particle dynamics, Procedia Comput. Sci. **18**, 2565 (2013).

[43] S. Plimpton, Fast parallel algorithms for short-range molecular dynamics, J. Comput. Phys. **117**, 1 (1995).

[44] A. Stukowski, Visualization and analysis of atomistic simulation data with OVITO – the open visualization tool, Modell. Simul. Mater. Sci. Eng. **18**, 015012 (2010).

[45] A. Boromand, S. Jamali, and J. M. Maia, Viscosity measurement techniques in dissipative particle dynamics, Comput. Phys. Commun. **196**, 149 (2015).

[46] N. Moreno, D. Moreno-Chaparro, F. Balboa Usabiaga, and M. Ellero, Hydrodynamics of spike proteins dictate a transport-affinity competition for SARS-CoV-2 and other enveloped viruses, Sci. Rep. **12**, 11080 (2022).

[47] D. Moreno-Chaparro, N. Moreno, F. B. Usabiaga, and M. Ellero, Computational modelling of passive transport of functionalized nanoparticles, J. Chem. Phys. **158**, 104108 (2023).

[48] J. Rotne and S. Prager, Variational treatment of hydrodynamic interaction in polymers, J. Chem. Phys. **50**, 4831 (1969).